frontiers | Frontiers in Mechanical Engineering

TYPE Original Research
PUBLISHED 03 December 2025
DOI 10.3389/fmech.2025.1707301



OPEN ACCESS

EDITED BY
Alessandro Ruggiero,
University of Salerno, Italy

REVIEWED BY
Mladen Radojković,
University of Priština in Kosovska Mitrovica, Serbia
Hang Zhao,
Fudan University, China

*CORRESPONDENCE
Xiongfei Yin,
yinxiongfei888@163.com

RECEIVED 17 September 2025
REVISED 22 November 2025
ACCEPTED 24 November 2025
PUBLISHED 03 December 2025

CITATION
Luo J, Chen Y, Cheng Y, Lin J, Wang Z and Yin X (2025) Study on robotic projectile launching based on multi-factor analysis and parameter optimization.
*Front. Mech. Eng.* 11:1707301.
doi: 10.3389/fmech.2025.1707301



# Study on robotic projectile launching based on multi-factor analysis and parameter optimization

Jiaming Luo[1,2], Yang Chen[1,2], Yijing Cheng[1,2], Jie Lin[1,2], Zhongge Wang[1,2] and Xiongfei Yin[1,2]*

[1]Hangzhou Institute for Advanced Study, University of Chinese Academy of Sciences, Hangzhou, China, [2]University of Chinese Academy of Sciences, Beijing, China

The precision of projectile launching mechanisms, which utilize counter-rotating friction wheels, is critical for system effec-tiveness. This study introduces a hybrid approach combining multi-physics simulation with an intelligent optimization algo-rithm to determine key design parameters. Initially, Finite Element Analysis (FEA) and kinematics simulations were conducted on a 3D model to generate a comprehensive dataset linking operational conditions to projectile dynamics. This dataset then served to train a neural network for velocity prediction. Subsequently, a genetic algorithm was implemented to optimize the friction coefficient and inter-wheel gap by targeting a desired exit velocity range. The proposed methodology successfully identifies optimal parameter configurations, offering a robust, data-driven solution to a complex design challenge.

KEYWORDS

**projectile launch, kinematic simulation, finite element analysis, neuralnetwork, parameter optimization**

## 1 Introduction

Advancements in robotics are prominently showcased in international robotics competitions (Buss Becker et al., 2024; Deng et al., 2025; Yepez-Figueroa et al., 2025). These contests feature clearly defined roles for various robot classes, exemplified by Unmanned Aerial Vehicles (UAVs) equipped with launching mechanisms tasked with deploying small projectiles (Zhang, 2025a). The competition framework incentivizes students to translate theoretical knowledge into practical applications, thereby fostering the extension of related technologies into sectors such as logistics and autonomous driving (Tian et al., 2025; Hwang et al., 2025). Concurrently, these events serve as crucial platforms for talent development within the robotics field, stimulating student innovation and creativity, and thus acting as significant catalysts for the advancement of robotics (Liu X. et al., 2024a; Lee et al., 2025).

Friction wheel systems represent the predominant launching mechanism employed in these international robotics competitions. The fundamental principle involves utilizing the high-speed rotation of two counter-rotating wheels to engage and accelerate the projectile, primarily through frictional force, facilitating kinetic energy transfer and enabling precise trajectory control (Zhang et al., 2024; Aparow et al., 2016). The core operational mechanism hinges upon the effective application of compressive and frictional forces to the projectile, which is crucial for ensuring it attains sufficient initial velocity for effective target engagement (Zhang X. et al., 2025a; Tang et al., 2025). However, in practical

applications and structural design, the performance of these systems is significantly influenced by several critical factors, notably the $d$ between the wheels, the coefficient of friction associated with the wheel material, and the wheel diameter (Silva-Rivera et al., 2021). Improper specification of any single parameter can lead not only to energy losses during acceleration but may also precipitate critical malfunctions, including jamming or trajectory deviations (misfiring), which significantly compromise the overall reliability of the launching system. For instance, setting the $d$ too small may subject the projectile to excessive compression, impeding smooth passage and potentially leading to system blockage or mechanical damage. Conversely, an excessively large distance results in insufficient contact force for effective frictional drive, causing inadequate exit velocity and consequently impairing impact effectiveness (Gao et al., 2025). Furthermore, an unduly low coefficient of friction increases the propensity for slippage during acceleration, diminishing kinetic energy transfer efficiency and preventing the projectile from attaining its nominal operational velocity. Therefore, determining the optimal solution amidst this complex interplay of interacting structural parameters represents the pivotal challenge in enhancing system performance (Liu Z. et al., 2024b; Guo et al., 2025).

Given that these mechanisms typically operate under extreme conditions—characterized by high speeds, high operational frequencies, and significant impact loads—even minor variations in structural parameters can induce highly non-linear, and potentially abrupt, effects on overall system performance (Tan et al., 2023; Gao and Yi, 2025; Li et al., 2025). Traditional parameter design methodologies often rely heavily on empirical rules and linear models, approaches that frequently prove inadequate when addressing the intricate dynamics of complex, non-linearly coupled systems (Rongzhou et al., 2025; Zhizhong et al., 2023; Li and Li, 2025). Consequently, exploring more rigorous, systematic, and efficient optimization strategies for performance modeling and critical parameter identification pertaining to the launching mechanism holds significant theoretical importance and substantial engineering value (Gao et al., 2024; Maxa et al., 2025; Lu et al., 2024).

This study originates from a robot manufacturing project. As an integral part of robot research and development, the launching mechanism is crucial to the R&D of the robot. We firmly believe that this research can provide inspiring ideas for future studies. 3D model simulation software serves as a crucial tool for conducting relevant research, enabling the simulation of complex physical phenomena. The Finite Element Method (FEM) is one of its core technologies, which can discretize and solve models to achieve accurate analysis of problems such as structural mechanics and electromagnetic fields. Based on this, optimization research aims to identify the optimal parameter combinations through optimization algorithms like genetic algorithms, thereby improving simulation accuracy and efficiency while reducing the consumption of computational resources. This approach holds significant application value in fields including engineering design and material processing (Nikolić et al., 2015; Gajević et al., 2024; Joksić et al., 2023; Zhang, 2025b). In this study, consideration was given to the fact that different software packages possess distinct advantages: ANSYS is suitable for finite element analysis, while ADAMS is more appropriate for kinematic simulation (Zhang and Ma, 2024; Liu et al., 2023; Xin et al., 2025; Srinivasarao et al., 2021; Serrao et al., 2021; Krenn and Schlicke, 2025). Therefore, finite element analysis (FEA) of the three-dimensional model for robotic projectile launching was conducted in ANSYS, and kinematic simulation was completed in ADAMS (Zikri et al., 2025). Through the application of neural network (NN) models, this work successfully overcomes the limitations inherent in traditional regression methods when dealing with high-dimensional, non-linear modeling challenges. The developed NN approach demonstrates the capacity to accurately predict key launch performance indicators across diverse design scenarios, even in the presence of complex physical constraints and parameter interdependencies (Zhou et al., 2025). Furthermore, this research elucidates the complex, non-linear, and interactive influences of the friction wheel's coefficient of friction and diameter on overall system performance. Optimizing the wheel diameter inherently involves navigating a trade-off between available structural space and the implications of the chosen friction coefficient. The adoption of a simulation data-driven modeling approach offers considerable advantages, not only reducing experimental expenditure and time investment but also markedly improving the resulting model's adaptability and generalization capacity for real-world engineering design tasks (Chen et al., 2025). Finally, an optimization and prediction model for launch velocity was established based on an adaptive genetic algorithm (AGA). Through the synergistic integration of the trained neural network with multi-objective optimization algorithms, this framework successfully identified optimal parameter combinations for the robotic launcher's friction wheels within specified operational ranges. This achievement results in a demonstrable improvement in the consistency and stability of the projectile's exit velocity (Zhang Z. et al., 2025b; Pu et al., 2025).

## 2 Description and launching principle of the projectile launching mechanism

In this study, the dimensions of the robotic system were reconstructed at a 1:1 scale using the professional modeling software SolidWorks. Meanwhile, the researchers assigned corresponding material parameters to the projectile and the launching mechanism respectively. Specifically, the projectile is made of thermoplastic polyurethane (TPU), while the launching mechanism is composed of polyurethane (PU) and aluminum alloy. These settings fully ensure the reliability of the three-dimensional model. The configuration of the robotic launching mechanism is illustrated in Figure 1a. It primarily comprises a projectile feeding conduit, two friction wheels, and a barrel. Notably, the friction wheels represent the most critical functional units (Figure 1b). Each individual friction wheel assembly consists of an electric motor, an aluminum alloy inner core, and an external Polyurethane (PU)

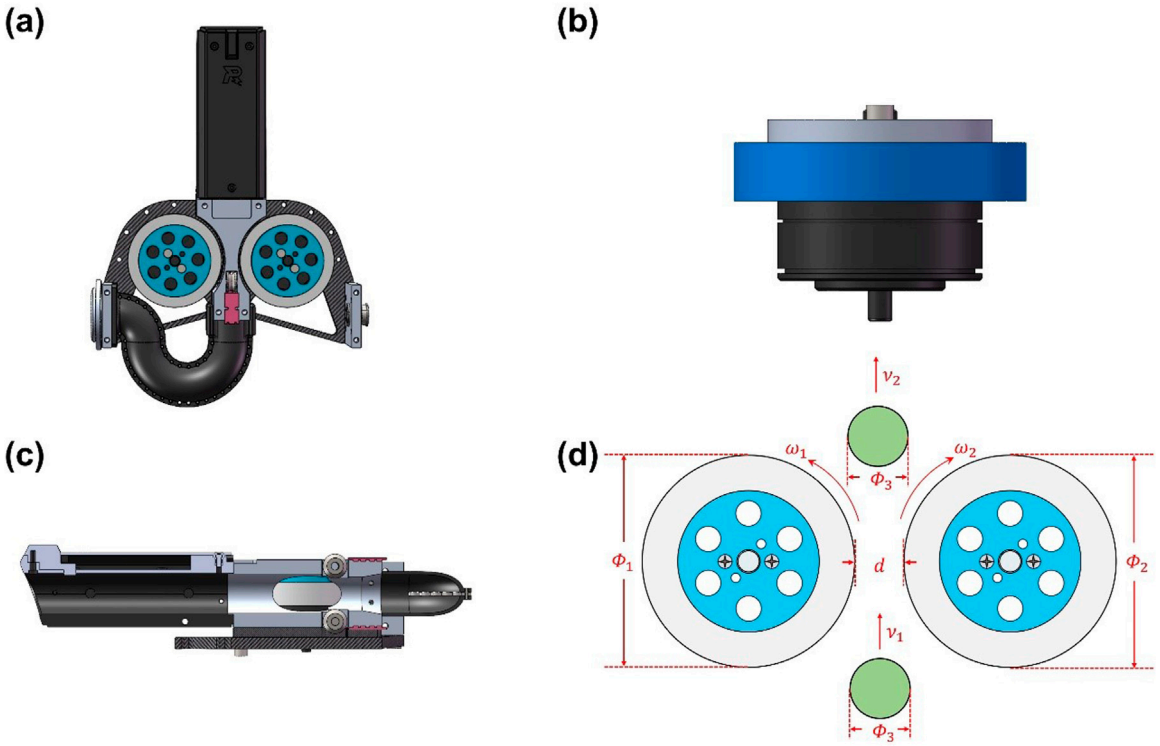


FIGURE 1
Model and schematic of the launching mechanism. **(a)** 3D model of the launching mechanism. **(b)** Structure of the friction wheel assembly. **(c)** Cross-sectional view of the launching mechanism. **(d)** Schematic diagram of the launching mechanism.

TABLE 1 Rubber coating of the friction wheel.

| Parameter | Value |
|---|---|
| Material type | PU |
| Inner diameter | 46 mm |
| Outer diameter | 60 mm |
| Density | 1.2e-06 kg/mm$^3$ |
| Poisson's ratio | 0.29 |
| Elastic modulus | 8.4 MPa |
| Bulk modulus | 6.6667 MPa |
| Shear modulus | 3.2558 MPa |

TABLE 2 Core of the friction wheel.

| Parameter | Value |
|---|---|
| Material type | Aluminum alloy |
| Outer diameter | 46 mm |
| Density | 2.7e-06 kg/mm$^3$ |
| Poisson's ratio | 0.33 |
| Elastic modulus | 68,900 MPa |
| Bulk modulus | 67,549 MPa |
| Shear modulus | 25,902 MPa |

cladding. The projectile material is TPU, which combines high strength and high elasticity. It has a high tensile strength, enabling it to withstand large launch impact forces without being easily damaged. At the same time, it has excellent elasticity and can quickly return to its original shape after being deformed by external forces, which is beneficial for maintaining the motion stability of the projectile. Moreover, it has extremely outstanding wear resistance and can endure multiple launch frictions during repeated contact and friction with components such as friction wheels. Material characteristic parameters for the PU cladding, the aluminum alloy core, and the projectile material are detailed in Table 1, Tables 2,3, respectively.

TABLE 3 Projectile.

| Parameter | Value |
|---|---|
| Material type | TPU |
| Outer diameter | 17 mm |
| Density | 1.25e-06 kg/mm$^3$ |
| Poisson's ratio | 0.49 |
| Elastic modulus | 48.5 MPa |
| Bulk modulus | 808.33 MPa |
| Shear modulus | 16.275 MPa |

Figure 1c presents a cross-sectional view of the launch mechanism. Miniature bearings are positioned above and below the anticipated projectile path between the two friction wheels, ensuring the projectile is effectively suspended upon initial contact with the wheels. The projectile launching sequence is depicted in Figure 1d. A projectile (shown in green) travels vertically upwards along a linear trajectory with a certain initial velocity until it reaches the central position between, and contacts, the left and right friction wheels. The left friction wheel rotates counterclockwise at a high angular velocity $\omega_1$, while the right friction wheel rotates clockwise at a high angular velocity $\omega_2$. As the projectile enters the space between and contacts the wheels, the opposing rotation directions (counterclockwise for the left, clockwise for the right) generate frictional forces based on the relative motion tendency at the contact interface. Specifically, the left wheel imparts an upward-left frictional force, and the right wheel imparts an upward-right frictional force onto the projectile. The synergistic effect of these frictional forces propels the projectile vertically upwards. In this modeling, a fixed robotic system is adopted, meaning the robot's launching mechanism is rigidly connected to the robot via bolts and other fasteners. During operation, the position and posture of the robot body remain stationary, and projectile launching is achieved solely through the movement of the extrusion module in the end effector. Through dynamic, kinematic, and body constraint models, this modeling clearly describes the entire process of the projectile from "extrusion to detachment".

According to Hertz contact theory, the contact deformation between the friction wheels and the projectile is directly related to the $d$ between the wheels. When this distance decreases, the compressive deformation experienced by the projectile and wheels increases, leading to an enlarged contact area A. An increased contact area enhances the effectiveness of the frictional force, governed by $F_f = \mu F$ (where $\mu$ is the coefficient of friction and $F$ is the normal load), allowing the projectile to receive a more substantial frictional driving force and thus experience greater acceleration. Conversely, if $d$ is excessively large, the resulting insufficient compression leads to a smaller contact area, diminishing the frictional drive exerted on the projectile and consequently reducing the exit velocity.

The derivation based on the Hertz contact model (specifically for sphere-cylinder contact in this approximation) relies on several assumptions: the materials are isotropic, and the deformation is small, implying the contact zone dimensions are significantly smaller than the overall dimensions of the contacting bodies.

Key geometric and mechanical parameters are defined as follows:

Radius of the spherical object (projectile):

$$R_3 = \Phi_3/2 \tag{1}$$

Radius of the cylindrical surface (friction wheel):

$$R_1 = \Phi_1/2 \tag{2}$$

Equivalent radius of curvature:

$$1/R = 1/R_1 + 1/R_3 \tag{3}$$

Effective (equivalent) elastic modulus, where $E_1$, $E_2$ are the Young's moduli and $\nu_1$, $\nu_2$ are the Poisson's ratios of the two contact materials:

$$E' = \frac{1}{2}\left( \frac{1-\nu_1^2}{E_1} + \frac{1-\nu_2^2}{E_2} \right) \tag{4}$$

Under a normal load $F$, the contact radius $a$ is calculated as:

$$a = \left(\frac{3FR}{4E'}\right)^{1/3} \tag{5}$$

Pressure distribution:

$$p_0 = \frac{3F}{2\pi a^2} \tag{6}$$

Pressure at an arbitrary radial distance $r$:

$$p(r) = p_0\sqrt{1-\frac{r^2}{a^2}} \tag{7}$$

Normal deformation (indentation depth):

$$\delta = \left(\frac{9F^2}{16E'^2R}\right)^{1/3} \tag{8}$$

Under static or quasi-static contact conditions, the system adheres to the momentum conservation equation:

$$\nabla \cdot \sigma + b = \rho\ddot{u} \tag{9}$$

where $\sigma$ is the stress tensor, $b$ is the body force vector, $\rho$ is the density, and $\ddot{u}$ is the acceleration vector. The Finite Element Method (FEM) typically solves this using its weak form:

$$\int_\Omega \delta u^T \rho \ddot{u} d\Omega + \int_\Omega \delta\varepsilon^T \sigma d\Omega = \int_{\Gamma_t} \delta u^T t d\Gamma \tag{10}$$

Given the soft nature of the TPU projectile, its behavior is appropriately represented using hyperelastic material models, such as the Mooney-Rivlin or Ogden models:

$$W = C_{10}(\bar{I}_1 - 3) + C_{01}(\bar{I}_2 - 3) \tag{11}$$

$$W = \sum_{i=1}^{N}\frac{\mu_i}{\alpha_i}\left(\lambda_1^{\alpha_i} + \lambda_2^{\alpha_i} + \lambda_3^{\alpha_i} - 3\right) \tag{12}$$

Contact forces can be calculated using methods like the Penalty Method, where the contact force $F_c$ is linearly proportional to the penetration depth $g$ and contact stiffness $k$:

$$F_c = k \cdot g \tag{13}$$

Frictional forces are governed by the Coulomb friction law, where the tangential friction force $F_t$ is limited by the normal force $F_n$ and the coefficient of friction $\mu$:

$$F_t \le \mu F_n \tag{14}$$

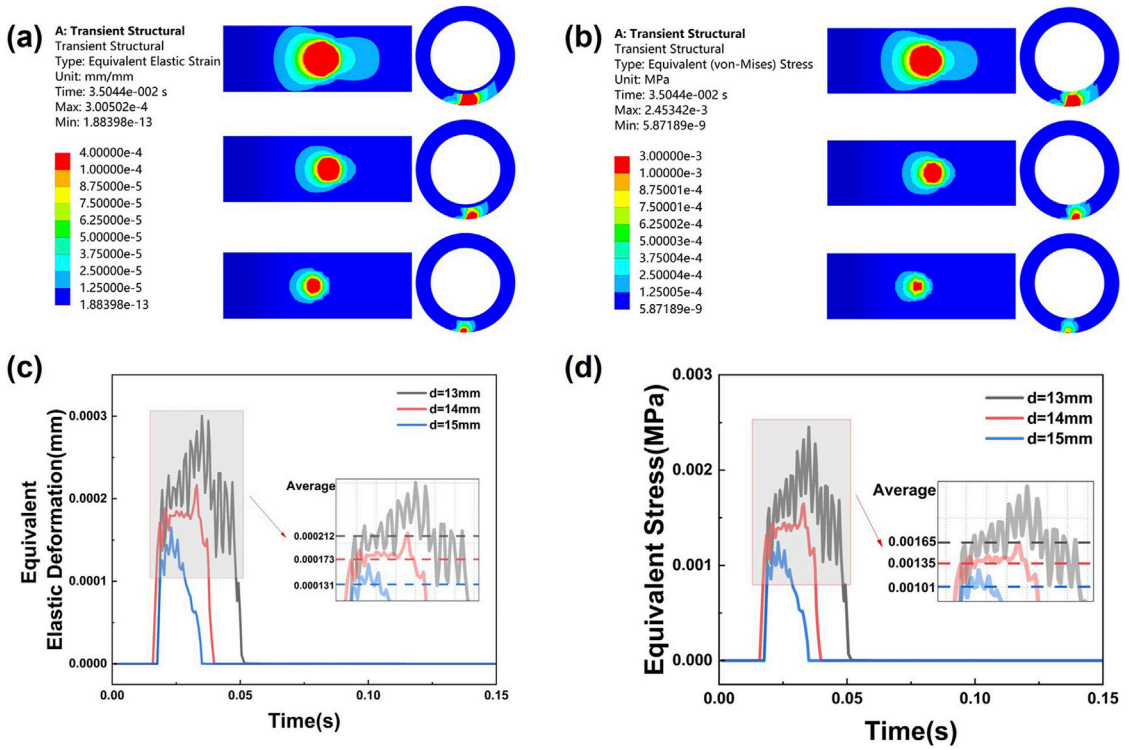


FIGURE 2
Simulation analysis of the effect of the *d* on launch dynamics. **(a)** Simulation contour plot of wheel strain for a given *d*. **(b)** Simulation contour plot of wheel stress for a given *d*. **(c)** Comparison of wheel strain at different *d*. **(d)** Comparison of wheel stress at different *d*.

To address the high-speed, highly non-linear dynamics characteristic of this problem, explicit integration methods are often employed. The central difference method is a common choice:

$$u^{n+1} = 2u^n - u^{n-1} + \Delta t^2 a^n \tag{15}$$

Analysis of the projectile's velocity change is conducted within the framework of Multibody Dynamics (MBD). The linear surface velocity of the friction wheels is given by:

$$v_{wheel} = \omega R \tag{16}$$

where $\omega$ is the angular velocity and $R$ is the wheel radius. Assuming the angular velocities of the left and right wheels are $\omega_1$ and $\omega_2$ respectively, the tangential frictional forces accelerate the projectile according to Newton's second law:

$$m\frac{dv}{dt} = F_{fric_1} + F_{fric_2} \tag{17}$$

Here, $F_{fric} = \mu F_n$, where the normal force $F_n$ arises from the compressive forces exerted by the wheels.

The velocity increase can also be related to the work done by friction through the work-energy theorem:

$$W = \int F_{fric} \cdot vdt = \frac{1}{2}mv^2 \tag{18}$$

# 3 Investigation of parameter effects on the projectile launching process

## 3.1 Influence of different parameters on mechanical characteristics during launch

This section details the mechanical simulation analysis of the projectile launching sequence. Owing to the inherent tendency for relative motion between the projectile and the high-speed rotating friction wheels, tangential frictional forces initiate on the wheel surfaces upon contact. Concurrently, the wheels experience radial compressive forces exerted by the projectile, leading to the development of stress concentrations within the contact interface. As interaction progresses, the contact area between the wheels and the projectile expands, causing a corresponding intensification of stress and strain levels within this zone. Finally, as the projectile nears disengagement from the wheels, the magnitude of the force it imparts diminishes, resulting in a subsequent reduction in the stress and strain experienced by the wheels.

### 3.1.1 Influence of friction wheel spacing on mechanical behavior during launch

The forces experienced by the friction wheels vary depending on the inter-wheel distance ($d$), as investigated for $d$ = 13 mm, $d$ = 14 mm, and $d$ = 15 mm. As illustrated in Figure 2, a smaller gap ($d$ = 13 mm) results in a greater compressive force exerted by the projectile onto the friction wheels. Consequently, this configuration exhibits a more rapid increase in stress and strain

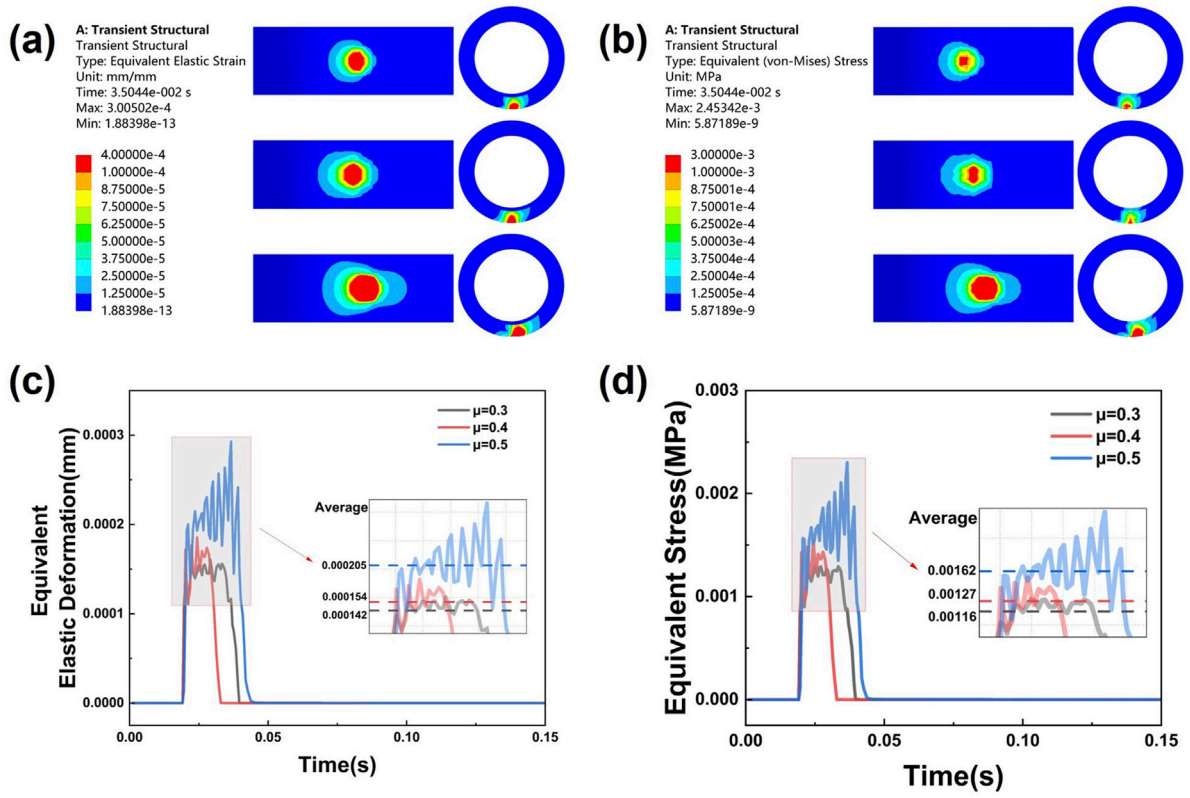


FIGURE 3
Simulation analysis of the effect of the coefficient of friction on launch dynamics. **(a)** Effect of friction coefficient on wheel strain. **(b)** Effect of friction coefficient on wheel stress. **(c)** Comparison of wheel strain at different coefficients of friction. **(d)** Comparison of wheel stress at different coefficients of friction.

within the contact zone, coupled with a more pronounced propagation of the high stress/strain region across the wheel surface and into its subsurface. Conversely, as the projectile approaches disengagement, the force imparted by it gradually diminishes, initiating a decline in the stress and strain levels. Examination of the stress/strain contour plots and associated data curves confirms this behavior: the magnitudes of stress and strain progressively decrease during the latter phase of the launch sequence, eventually returning to relatively low baseline levels after the projectile has fully separated.

### 3.1.2 Influence of friction coefficient on mechanical behavior during launch

The continued upward movement of the projectile leads to an expansion of the contact patch on the friction wheels. These wheels are subjected to a dual loading condition: radial compression from the projectile and tangential friction resisting their rotation. Stress and strain concentrate prominently at the contact interface, propagating into the wheel material while diminishing distance from the contact center. The entire contact-compression-disengagement cycle induces a dynamic stress-strain response within the wheels, characterized by an initial build-up, subsequent variations reflecting changing contact dynamics, and a final decrease upon projectile exit. This results in a characteristic time-dependent stress/strain curve showing an initial rise, intermediate fluctuations, and a concluding fall. The coefficient of friction $\mu$ significantly influences this mechanical response. Elevated $\mu$ values (illustrated by $\mu$ = 0.5) intensify the loading conditions, leading to increased peak stress and strain magnitudes and wider distribution of these high levels within the wheels. This trend is evident where higher $\mu$ generally corresponds to greater peak stress/strain and a larger affected volume. Figure 3 provides visual confirmation, showing substantially greater equivalent stress and equivalent elastic strain for $\mu$ = 0.5 relative to the $\mu$ = 0.3 and $\mu$ = 0.4 cases.

## 3.2 Influence of key parameters on projectile launch kinematics

The focus of this chapter is the kinematic behavior of the launching mechanism, examined through simulation. The distance between friction wheels, friction coefficient, material density of friction wheels, and elastic modulus of friction wheels may all affect the projectile's exit velocity. Through analysis, the distance between friction wheels and the friction coefficient have a relatively significant impact on the projectile's exit velocity, while the other two factors exert a minor influence. Therefore, this study mainly explores the effects of the distance between friction wheels and the friction coefficient on the projectile's exit velocity. A 3D model of the assembly was constructed and then utilized within a kinematics simulation software package. Through these simulations,

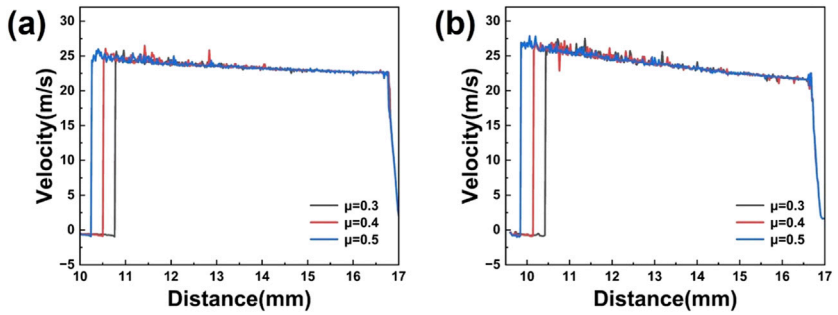


FIGURE 4
Effects of wheel geometry and spacing on projectile exit velocity. **(a)** Effect of varying wheel diameter with a fixed center-to-center distance on exit velocity. **(b)** Effect of varying center-to-center distance with a fixed wheel diameter on exit velocity.

the study systematically evaluated the impact of key geometric variations: the effect of the friction wheel $d$ on launch velocity; the consequences of unequal wheel diameters (single-wheel asymmetry) for both launch velocity and trajectory deviation velocity; and the influence of offset mounting hole positioning on these performance indicators. It was determined that excessive $d$ between wheels results in poor contact and diminished friction, hindering projectile acceleration. Insufficient $d$, conversely, causes over-compression and obstructs projectile passage, preventing ejection. Discrepancies in wheel diameters lead to differing surface velocities and asymmetric forces on the projectile, consequently lowering the exit velocity and inducing lateral motion (deviation velocity). Moreover, non-concentric or misaligned mounting disrupts the uniformity of contact pressure and deformation, introduces lateral forces, and destabilizes the projectile's trajectory, negatively affecting exit velocity, accuracy, and generating deviation velocity.

### 3.2.1 Effect of friction wheel spacing on exit velocity

The relationship between friction wheel spacing and projectile launch velocity was investigated under two distinct conditions modifying the $d$. The first condition involved varying the friction wheel diameters $\Phi$ while maintaining a fixed center-to-center distance, thus inversely relating $\Phi$ to $d$. The resulting exit velocity *versus* $d$ characteristics for coefficients of friction $\mu$ = 0.3, 0.4, and 0.5 are presented in Figure 4a. The second condition maintained constant wheel diameters but varied the center-to-center distance, directly correlating this distance with the radial gap $d$. Figure 4b illustrates the corresponding exit velocity *versus* $d$ relationships for the same $\mu$ values under this second condition.

Comparative analysis of Figures 4a,b indicates strikingly similar trends relating exit velocity to the $d$ in both approaches. Both configurations demonstrate that excessively narrow gaps prevent projectile ejection, while overly wide gaps yield insufficient exit velocities. Additionally, higher coefficients of friction generally broaden the range of operable gap distances. Nonetheless, minor differences are apparent. The minimum operable gap for launch is slightly smaller in the first condition ($d$ = 10.44 mm) compared to the second ($d$ = 10.78 mm), implying launch initiation may be less constrained when adjusting diameters at fixed centers. Considering exit velocities greater than 20 m/s as satisfactory, the effective operational range for $d$ is [10.44 mm–16.68 mm] under the first condition and [10.78 mm–16.8 mm] under the second. Crucially, evaluating the range of exit velocities achieved across the launchable $d$ intervals reveals that the second condition (adjusting center distance, fixed diameter) produces a smaller velocity variation than the first. This suggests that manipulating the center distance offers superior stability and consistency in the projectile's exit velocity compared to altering wheel diameters.

### 3.2.2 Effect of diameter mismatch on exit and lateral deviation velocity

Disparities in friction wheel diameters $\Phi$ influence not only the projectile's exit velocity but also induce lateral trajectory deviations. If the wheel diameters differ while operating at identical angular velocities ($\omega_1 = \omega_2$), their peripheral linear speeds ($v = \omega r$) will inevitably be unequal ($v_1 \neq v_2$). Given that the effectiveness of the frictional force ($F_f = \mu F$) relates to the surface velocity at the contact interface, the driving forces applied by each wheel become asymmetric. Specifically, the wheel with the larger diameter possesses a higher linear speed and exerts a stronger tangential driving force on the projectile, whereas the smaller-diameter wheel provides a weaker impulse. This imbalance precludes symmetric and balanced acceleration, thereby reducing the overall efficiency of work done by friction and lowering the resultant exit velocity.

Regarding the impact on projectile deviation velocity: unequal wheel diameters generate an unbalanced force system acting on the projectile, resulting in a net lateral force component. The larger-diameter wheel contributes a greater lateral component to the total frictional force, compelling the projectile to deviate towards the side with the smaller-diameter wheel. This sustained lateral force imparts an additional transverse velocity component (deviation velocity) to the projectile during ejection, causing its trajectory to diverge from the intended linear path. The magnitude of this deviation velocity is positively correlated with the difference in wheel diameters; a larger diameter discrepancy leads to a more significant lateral force component, a higher deviation velocity, and consequently, poorer directional accuracy upon exit.

In the specific scenario where wheel diameters are inconsistent but their center positions remain fixed, the projectile first engages the larger-diameter wheel before contacting the smaller one. This non-simultaneous contact ensures that the resultant horizontal force acting on the projectile is not aligned with the desired launch axis,

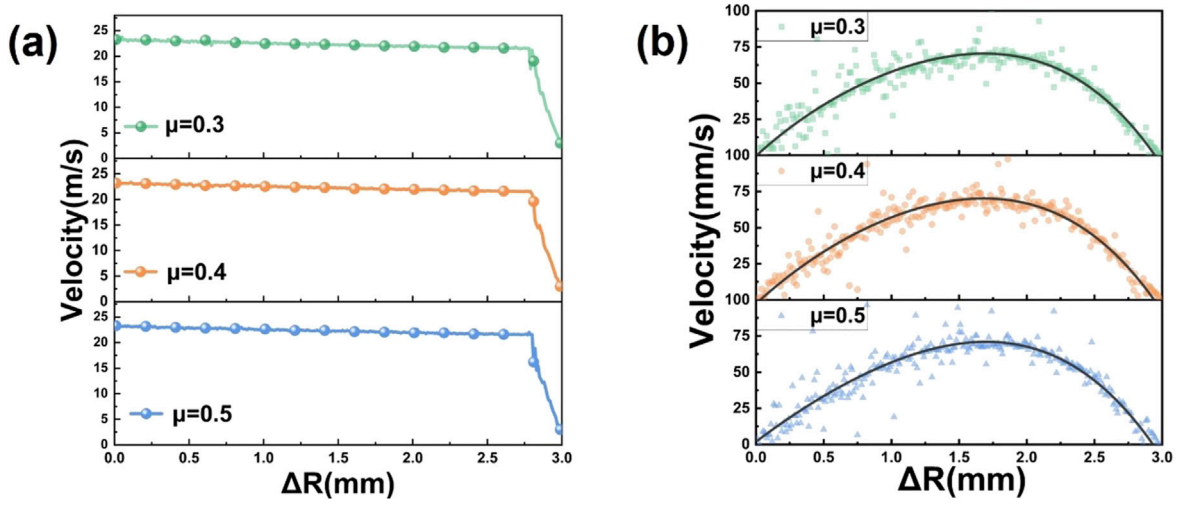


FIGURE 5
Effect of friction wheel diameter difference on projectile exit and deviation velocities. **(a)** Effect of diameter difference on projectile exit velocity. **(b)** Effect of diameter difference on projectile deviation velocity.

influencing the exit velocity while simultaneously generating a horizontal deviation velocity. Simulations were conducted under these fixed-center conditions, varying the diameter of one wheel to create a radius difference. Figure 5a illustrates the relationship between projectile exit velocity and this radius difference for three coefficients of friction ($\mu$ = 0.3, 0.4, 0.5). As the radius difference increases, the $d$ between the wheels also widens. This widening gap is the primary reason for the observed progressive decrease in exit velocity as the radius difference grows. Figure 5b presents the corresponding relationship between deviation velocity and the radius difference. Initially, with identical radii (zero difference), the compressive forces are balanced, and the deviation velocity is zero. As the radius difference grows, the force imbalance introduces a deviation velocity. However, the concurrent increase in the $d$ progressively reduces the overall compressive force exerted on the projectile. When the gap $d$ approaches the projectile diameter Φ, the compressive interaction significantly weakens, causing the deviation velocity to diminish back towards zero. Consequently, the projectile's deviation velocity exhibits a non-monotonic trend as the radius difference increases initially due to increasing force asymmetry, then falls as the effect of the widening gap and reduced overall compression becomes dominant.

### 3.2.3 Effect of relative wheel-projectile position on exit and deviation velocity

Asymmetric positioning of the two friction wheels relative to the projectile's intended path results in non-simultaneous contact. During the compression and launch sequence, the projectile engages one wheel initially and disengages from the other wheel finally. This temporal asymmetry inevitably precludes a balanced and symmetric acceleration, leading to lateral deviation in the projectile's trajectory. The influence of this asymmetric positioning on projectile exit velocity and deviation velocity was investigated under two distinct conditions.

Condition 1: Constant $d$. Maintaining a fixed gap distance between the wheels, simulations were performed varying the lateral offset distance for three coefficients of friction ($\mu$ = 0.3, 0.4, 0.5). Figure 6a illustrates the relationship between exit velocity and wheel offset distance. It is observed that, across the different friction coefficients, the exit velocity consistently fluctuates around approximately 23 m/s, indicating that the offset distance exerts only a marginal influence on the exit velocity under these conditions. Conversely, Figure 6b shows the relationship between deviation velocity and wheel offset distance. The deviation velocity demonstrates a clear positive correlation with the offset distance, increasing progressively as the offset becomes larger. Notably, this increasing trend appears quantitatively similar for all three coefficients of friction.

Condition 2: Constant Coefficient of Friction. Here, the coefficient of friction was held constant while simulations were running varying the offset distance for three different $d$ ($d$ = 13 mm, $d$ = 14 mm, $d$ = 15 mm). Figure 6c presents the exit velocity as a function of offset distance for these gaps. As anticipated, a smaller gap imparts greater compressive friction, resulting in higher exit velocities; thus, the velocities follow the trend $V_{d=13mm} > V_{d=14mm} > V_{d=15mm}$. Figure 6d depicts the deviation velocity *versus* offset distance under these conditions. For all three gap settings, the deviation velocity increases monotonically with increasing offset distance. Furthermore, at any given offset distance, a smaller $d$ leads to a larger deviation velocity, maintaining the comparative trend $V_{d=13mm} > V_{d=14mm} > V_{d=15mm}$.

## 4 Predictive model development and launch velocity optimization using an adaptive genetic algorithm

In practical applications, the ability to accurately predict the launch velocity generated by the friction wheels holds significant reference value for preventative equipment maintenance and

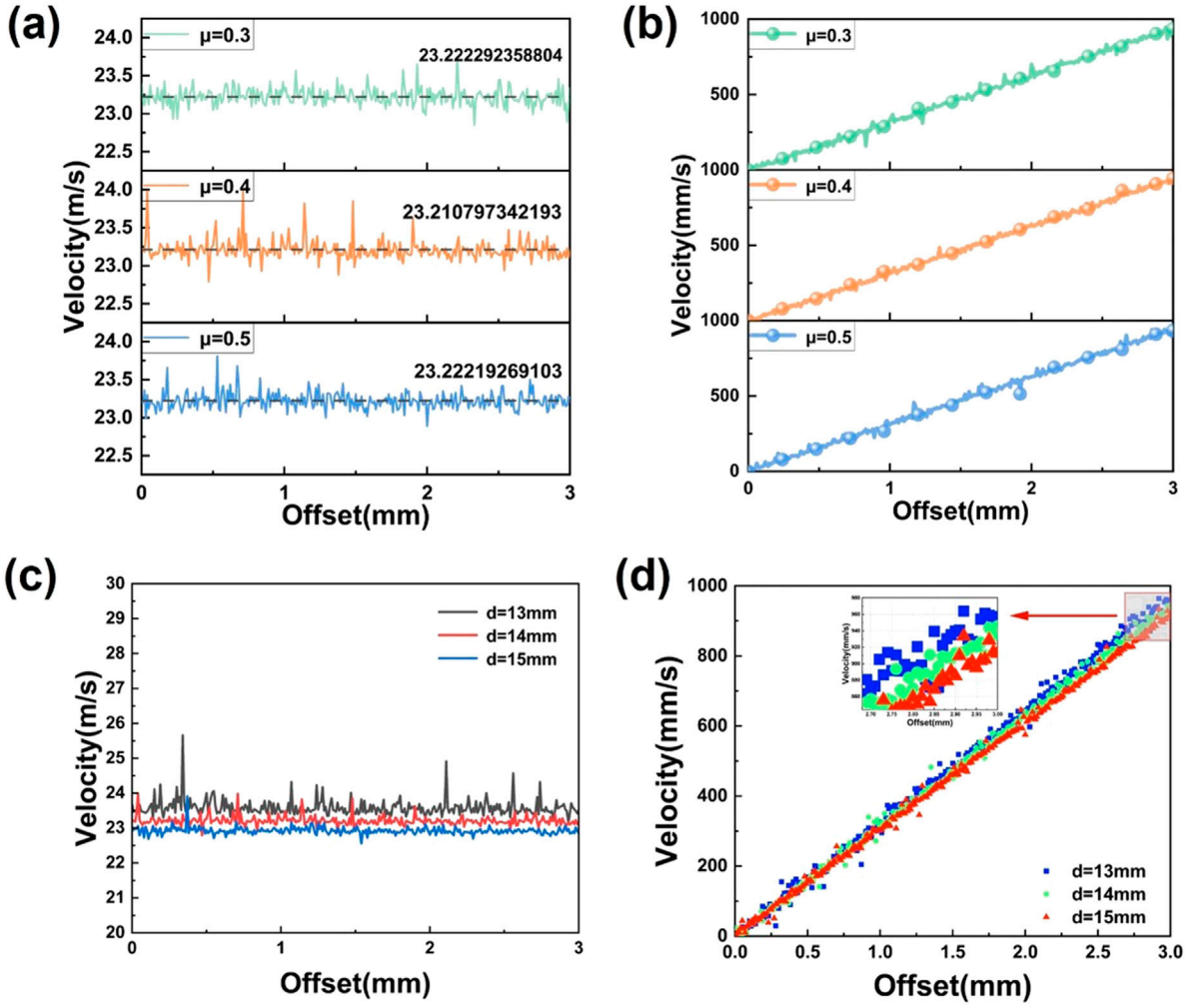


FIGURE 6
Impact of lateral wheel misalignment on projectile exit and deviation velocities. **(a)** Relationship between exit velocity and offset distance under a constant *d*. **(b)** Relationship between deviation velocity and offset distance under a constant *d*. **(c)** Relationship between exit velocity and offset distance under a constant friction coefficient. **(d)** Relationship between deviation velocity and offset distance under a constant friction coefficient.

enhancing operational accuracy (hit rate). While various predictive modeling techniques are commonly employed, including Multilayer Perceptron (MLP) and other machine learning or neural network architectures, this study initially focused on developing a launch velocity prediction model using friction wheel gap, coefficient of friction, and wheel radius as input variables (illustrated in Figure 7). To achieve efficient and accurate data training, this study adopts a neural network model and conducts targeted design of core structural parameters based on a comprehensive consideration of model fitting performance and generalization ability. Regarding the hidden layer configuration, a two-layer architecture is ultimately determined: while a single hidden layer features a simple structure, it struggles to capture complex features in the data and carries a significant risk of underfitting; in contrast, three or more hidden layers tend to cause the model to learn redundant information, increasing the probability of overfitting. Therefore, the two-layer hidden layer represents the optimal choice that balances fitting effectiveness and model stability. The selection of the activation function and loss function is also centered on research requirements: the ReLU function is employed as the activation function, which not only effectively mitigates the vanishing gradient problem to ensure the stability of the training process but also offers the advantage of high computational efficiency, capable of accelerating the model training speed. For the loss function, Mean Squared Error (MSE) is selected due to its high sensitivity to data errors, enabling precise quantification of the deviation between predicted values and true values, which is highly consistent with the study's requirements for prediction accuracy. In terms of data partitioning, to ensure training effectiveness and evaluation reliability, the dataset is divided into a training set, validation set, and test set at a ratio of 8:1:1. Specifically, the training set, accounting for 80% of the total data, is used for the core learning of model parameters; the 10% validation set is utilized for hyperparameter tuning and performance monitoring during the training process; and the remaining 10% test set is employed for the independent evaluation of the model's final generalization ability, and the model training results are shown in Figure 8. Analysis of the

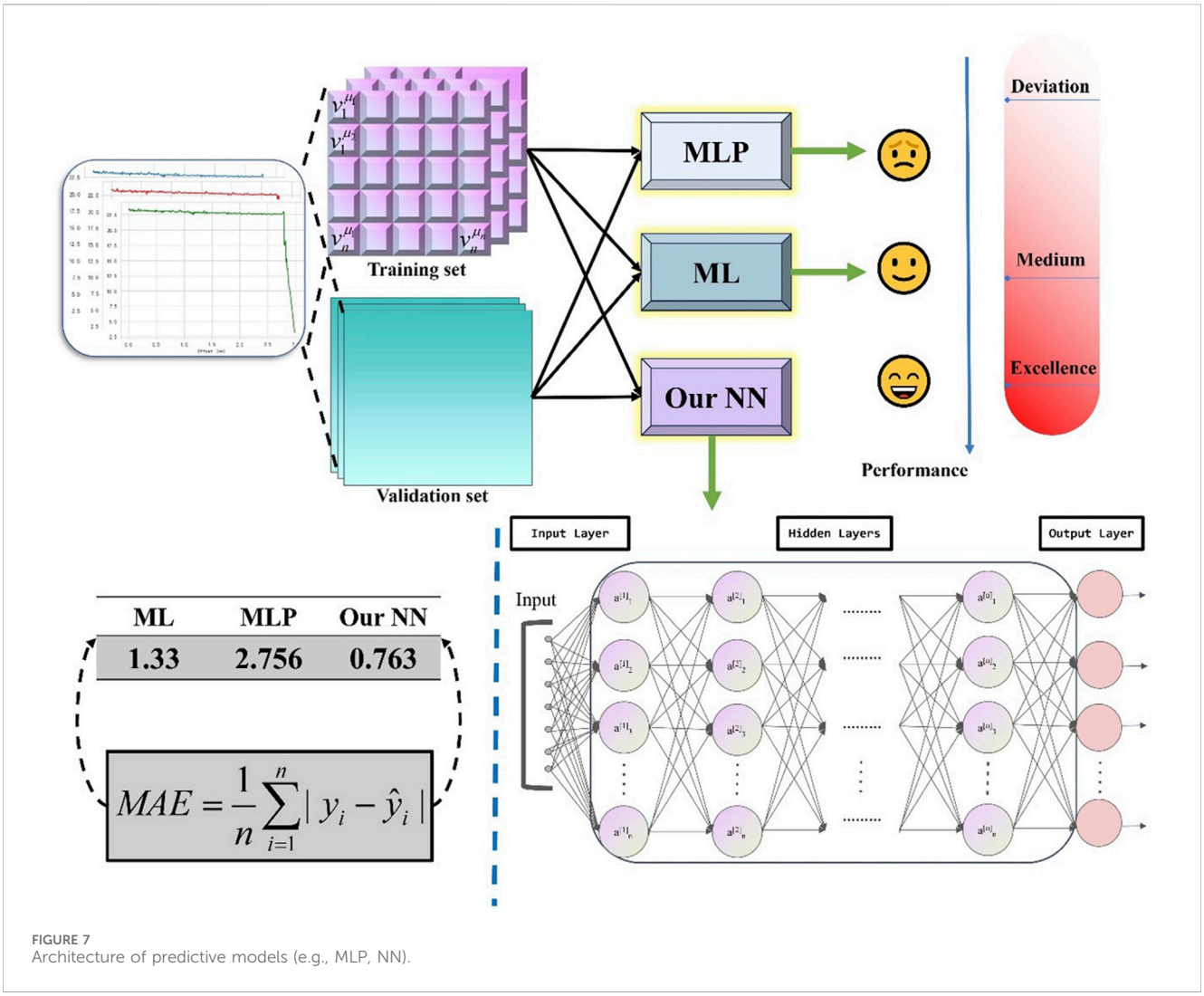


FIGURE 7
Architecture of predictive models (e.g., MLP, NN).

experimental data indicated that this initial model performed adequately on the provided dataset, achieving prediction errors within the range of 0.76 m/s to 1.33 m/s, thus demonstrating reasonable predictive capability. However, a critical limitation of such conventional models is their inability to determine the specific input parameter settings required to achieve a desired target launch velocity. This restricts their applicability in complex real-world scenarios where parameter optimization is essential. To address this deficiency, the present work introduces an Adaptive Genetic Algorithm (AGA) specifically designed to predict not only the resulting launch velocity but also the corresponding input parameter configuration needed to produce it.

The conventional Genetic Algorithm (GA) framework implemented in this study incorporates the following key modifications to enhance its performance and applicability. As shown in Figure 9.

- Instead of relying on a potentially complex physical model, this approach employs an empirical average, denoted as $\hat{v} = \frac{1}{k}\sum v_j$, as a surrogate. Utilizing this surrogate obviates the need for intricate first-principles modeling and enhances the algorithm's adaptability, particularly in scenarios characterized by limited data samples.
- A piecewise fitness function, denoted as $f(X)$, is utilized. This function applies differential evaluation criteria to candidate solutions depending on whether they fall inside or outside a predefined target interval. Such a strategy effectively guides the population's convergence towards the desired region, thereby enhancing the algorithm's capability for directed search within that specific objective range.

$$f(\mathrm{X}) = \begin{cases} \dfrac{1}{1+\left|\hat{v}-v_{target}\right|}, v_{min} < \hat{v} < v_{max} \\ -\left|\hat{v}-v_{target}\right|, otherwise \end{cases} \tag{19}$$

- The algorithm employs advanced genetic operators, pairing the hybrid Blend Crossover ($BLX-\alpha$) strategy with a tournament selection mechanism. In comparison to conventional single-point crossover and simpler selection techniques, this combination demonstrates superior suitability for continuous parameter optimization tasks, achieves faster convergence rates, and more effectively

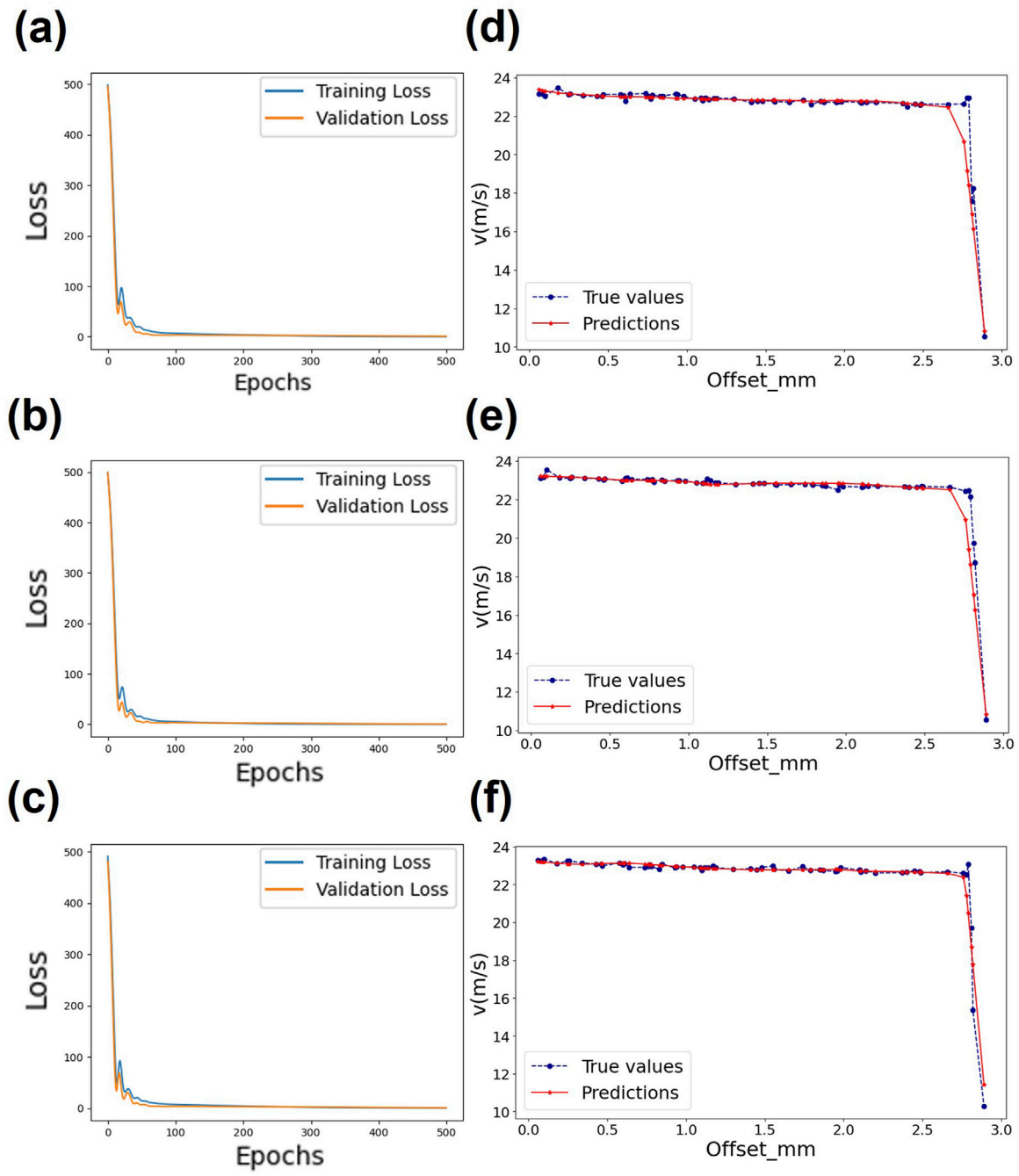


FIGURE 8
Neural Network training performance (e.g., loss vs. epoch). **(a)** shows the model training results when μ = 0.5; **(b)** shows the model training results when μ = 0.4; **(c)** shows the model training results when μ = 0.3; **(d)** shows the model validation results when μ = 0.5; **(e)** shows the model validation results when μ = 0.4; **(f)** shows the model validation results when μ = 0.3.

maintains population diversity throughout the evolutionary process.

- The implemented cascaded optimization methodology simultaneously refines the coefficient of friction $\mu$ and the $d$. A key advantage of this technique is its integration of local search data into the global optimization process, which effectively prevents premature convergence to suboptimal local solutions.

$$\hat{v}(x) = \mathrm{E}[v|Nearest_k(x)|] \tag{20}$$

$$f(\mathrm{X}) = g(\hat{v}(x)) \tag{21}$$

Due to the friction wheels squeezing and launching the projectile, an excessively high rotational speed may excessively consume the motor of the friction wheels, leading to motor burnout, while an excessively low projectile exit velocity will result in failure to meet the normal launch requirements.

TABLE 4 Prediction effect of adaptive genetic algorithm.

| $v_{target}$ (m/s) | $d$ (mm) | $\mu$ | $v_{p-GA}$ (m/s) | $AE_{GA}$ (m/s) | $d$ (mm) | $\mu$ | $v_{p-AGA}$ (m/s) | $AE_{AGA}$ (m/s) | $MAE_{GA}$ (m/s) | $MAE_{AGA}$ (m/s) |
|---|---|---|---|---|---|---|---|---|---|---|
| 22.02 | 15.66 | 0.46 | 22.11 | 0.09 | 15.84 | 0.47 | 22.08 | 0.06 | 0.44 | 0.28 |
| 22.08 | 15.60 | 0.47 | 22.19 | 0.11 | 15.79 | 0.49 | 22.18 | 0.10 | | |
| 22.14 | 15.79 | 0.46 | 22.11 | 0.03 | 15.96 | 0.37 | 21.95 | 0.19 | | |
| 22.20 | 15.93 | 0.42 | 21.97 | 0.23 | 15.67 | 0.48 | 22.19 | 0.01 | | |
| 22.76 | 15.75 | 0.48 | 24.64 | 1.88 | 15.82 | 0.47 | 21.97 | 0.79 | | |
| 22.82 | 15.53 | 0.38 | 22.25 | 0.57 | 15.54 | 0.43 | 22.32 | 0.50 | | |
| 22.88 | 15.30 | 0.48 | 22.32 | 0.56 | 15.30 | 0.30 | 22.45 | 0.43 | | |
| 23.00 | 14.65 | 0.35 | 22.96 | 0.04 | 14.64 | 0.45 | 22.88 | 0.12 | | |

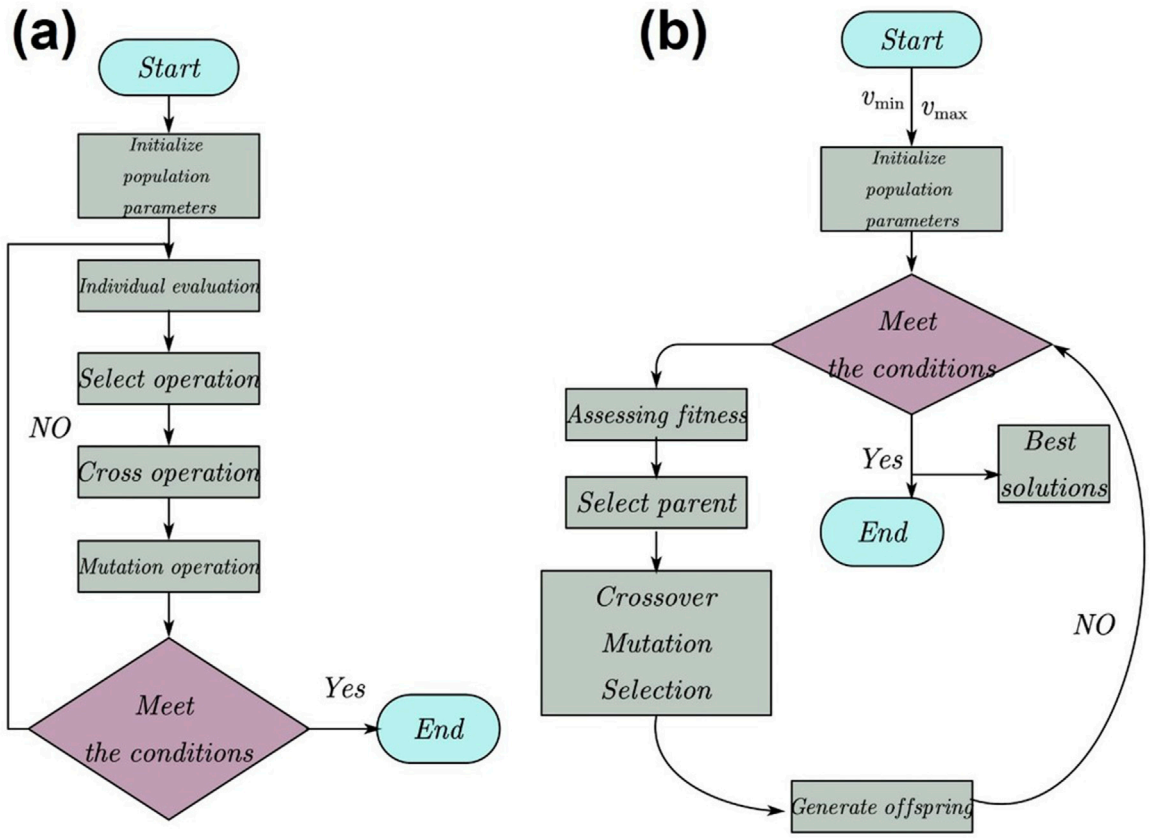


FIGURE 9
Performance comparison between the Traditional and Adaptive Genetic Algorithms. Genetic Algorithms **(a)** and Adaptive Genetic Algorithms **(b)**.

According to the optimal range of projectile exit velocity specified in the competition, which is 22 m/s – 23 m/s, the optimization objective of this study is set to $v_{target}$. To achieve this optimal velocity range, optimal parameter sets are first predicted by the two algorithms, and subsequently, these predicted parameter combinations are validated through simulation. The experimental results, summarized in Table 4, indicate that the GA yielded a mean error of 0.44, whereas the AGA achieved a significantly lower mean error of 0.28. The validation thus confirms that the parameter configurations generated by the AGA model are more effective, resulting in smaller velocity errors and demonstrating the model's superior predictive capability.

Following the optimization process, the actual launching mechanism was adjusted according to the optimal parameters derived, as illustrated in Figure 10. Subsequently, projectile launch tests were conducted to acquire experimental data. A comparison between the collected test data and the simulation prediction data revealed a close correspondence, thereby

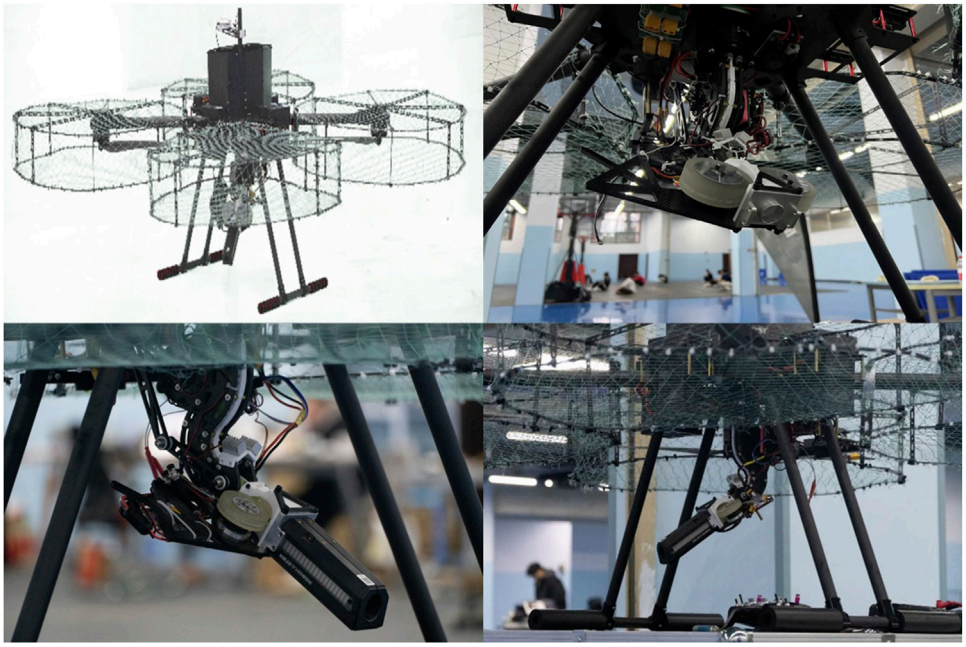

FIGURE 10
The experimental prototype of the launching mechanism.

validating the feasibility and effectiveness of the proposed model and algorithm.

## 5 Conclusion

Key factors influencing stress and strain experienced by the friction wheels include $d$ and $\mu$. Decreasing $d$ demonstrably increases the maximum stress and strain, while employing a higher coefficient of friction $\mu$ likewise leads to greater peak stress and strain levels.

Projectile performance is also directly impacted. Exit velocity tends to increase with tighter $d$ and a higher $\mu$. In contrast, the magnitude of the deviation velocity (lateral offset speed) is positively correlated with both the degree of misalignment in the friction wheel mounting positions and the extent of the difference between the two wheel radii.

An improved Adaptive Genetic Algorithm (AGA) is presented herein to address these relationships. Compared with existing research on the optimization of robotic launching mechanisms, the advantages and innovations of this study lie in the adoption of an optimization scheme combining neural networks with genetic algorithms, which is a highly innovative optimization method. Key features include cascaded optimization of $\mu$ and $d$; a piecewise fitness function for targeted search; and a blend crossover strategy for enhanced exploration. These modifications significantly boost search efficiency and the algorithm's capacity for global optimization. Experiments verify the model's high predictive accuracy (low error) and its direct utility in identifying parameter sets needed to attain specific target velocities. Consequently, this research delivers a precise, data-informed optimization framework for launcher design, offering a robust solution to the intricate problem of multi-parameter optimization in complex nonlinear systems.

## 6 Limitations and future outlook

The optimal parameter combinations output by the genetic algorithm in this study are derived under an idealized premise: it is assumed that no wear occurs at the contact interface between the friction wheels and the projectile during the transient process of projectile launching. Although the wear effect of materials is unavoidable in the actual dynamic meshing process, the core objective of this study is to establish a baseline performance model and a parameter optimization framework for the launching system. Therefore, as a reasonable preliminary simplification, the time-varying wear effect has not been incorporated into the current model. This treatment allows us to focus on the direct impact of core parameters on the stability of the initial launching velocity. On this basis, future research can integrate the Archard wear model, which is well-established in the field of friction and wear, into the existing framework. Owing to its wide applicability, this model has been extensively employed in the wear prediction of friction pairs, such as metal matrix composites and molds. The core formula of the Archard wear model is $W = K\frac{FS}{H}$, where $W$ is the wear volume, $K$ is the wear coefficient, $F$ is the contact pressure, $S$ is the relative sliding distance, and $H$ is the hardness of the softer material. The wear coefficient $K$ in the model will be obtained through pin-on-disk friction and wear tests: material pairs consistent with the actual friction wheels (PU) and projectiles (TPU) will be selected, and the wear behaviors under different contact pressures and sliding speeds will be simulated on a friction tester. The $K$ value will be derived by fitting after calculating the wear volume via the weight loss method. The contact pressure $F$ will be extracted from the stress analysis results of the

existing multi-physics simulation, with a focus on collecting the distributions of maximum and average contact pressures in the contact area between the friction wheels and the projectile. The relative sliding distance $S$ will be accurately calculated through a kinematic model by combining the rotational speed of the friction wheels and the contact time. Considering the transient variation characteristics of contact pressure and sliding speed during the actual launching process, the construction idea of the dynamic wear model will be referred to. Specifically, the static wear coefficient $K$ will be optimized into a function that dynamically changes with contact pressure and relative sliding speed. Meanwhile, combined with the fatigue hardening characteristics of the friction wheel material, a surface hardness $H$ curve that varies with wear depth will be introduced to make the model more consistent with actual working conditions. Through this scheme, future research can deeply explore the influence of the wear effect on the long-term performance and parameter robustness of the system, clarify the retention ability of the optimal parameters under wear conditions, and provide a quantitative basis for the regular maintenance cycle and material selection optimization of the friction wheels. This will enable the parameter optimization results of this study to be more in line with the practical engineering requirements.

Although the practical application of the optimal friction wheel parameters may face the issue that wear between the projectile and friction wheels leads to changes in the actual distance between the friction wheels, the parameter optimization method proposed in this study still holds significant academic value and represents a meaningful phase of progress. Firstly, this method clarifies the coupling laws between parameters through theoretical modeling, providing a design basis for subsequent research. Secondly, the optimization results reveal the limitations of traditional empirical parameters, promoting the paradigm shift in the industry from the "trial-and-error method" to model-driven design. Finally, the parameter analysis framework established in this study can guide engineers in prioritizing parameters under constrained conditions. The improvement of such systematic understanding serves as a key cornerstone for supporting the sustainable development of the friction transmission field.

## Data availability statement

The original contributions presented in the study are included in the article/supplementary material, further inquiries can be directed to the corresponding author.

## Author contributions

JaL: Conceptualization, Data curation, Formal Analysis, Investigation, Methodology, Project administration, Software, Writing – original draft, Writing – review and editing. YaC: Conceptualization, Data curation, Investigation, Methodology, Software, Writing – original draft. YiC: Data curation, Formal Analysis, Software, Writing – original draft. JeL: Methodology, Supervision, Validation, Writing – review and editing. ZW: Supervision, Validation, Writing – review and editing. XY: Supervision, Writing – review and editing.

## Funding

The authors declare that no financial support was received for the research and/or publication of this article.

## Conflict of interest

The authors declare that the research was conducted in the absence of any commercial or financial relationships that could be construed as a potential conflict of interest.

## Generative AI statement

The authors declare that Generative AI was used in the creation of this manuscript. The author(s) declare that Generative AI was used in the creation of this manuscript. Portions of the written content in this manuscript were generated or edited with the assistance of OpenAI's ChatGPT (GPT-4 model). The tool was used to improve language clarity and structure. All content was critically reviewed and approved by the authors.

Any alternative text (alt text) provided alongside figures in this article has been generated by Frontiers with the support of artificial intelligence and reasonable efforts have been made to ensure accuracy, including review by the authors wherever possible. If you identify any issues, please contact us.

## Publisher's note



## References

Aparow, V. R., Hudha, K., Kadir, Z. A., Amer, N. H., Abdullah, S., and Megat Ahmad, M. M. (2016). Identification of an optimum control algorithm to reject unwanted yaw effect on wheeled armored vehicle due to the recoil force. *Adv. Mechanical Engineering* 9 (1), 1687814016683350. doi:10.1177/1687814016683350

Buss Becker, L., Downs, A., Schlenoff, C., Albrecht, J., Kootbally, Z., Ferrando, A., et al. (2024). Effects of the human presence among robots in the ARIAC 2023 industrial automation competition. *J. Intelligent and Robotic Syst.* 110 (3), 112. doi:10.1007/s10846-024-02148-6

Chen, Z., Cui, Y., Cai, H., Zheng, H., Ning, Q., and Ding, X. (2025). Multi-objective optimization of photovoltaic facades in prefabricated academic buildings using transfer learning and genetic algorithms. *for Carbon Emissions, Daylighting, and Thermal Comfort Energy* 328, 136470. doi:10.1016/j.energy.2025.136470

Deng, H., Huang, Z., Wu, J., Güneri, F., Shen, Z. Y., and Yu, C. (2025). Harnessing the power of industrial robots for green development: evidence from China's manufacturing industry. *Technol. Forecast. Soc. Change* 215, 124099. doi:10.1016/j.techfore.2025.124099

Gajević, S., Miladinović, S., Güler, O., Özkaya, S., and Stojanović, B. (2024). Optimization of dry sliding wear in hot-pressed Al/B4C metal matrix composites using taguchi method and ANN. *Materials* 17 (16), 4056. doi:10.3390/ma17164056

Gao, Z., and Yi, W. (2025). Prediction of projectile impact points and launch conditions based on extreme learning machine. *Measurement* 252, 117308. doi:10.1016/j.measurement.2025.117308

Gao, S., Shi, Y., Ye, P., Zhang, S., and Pan, G. (2024). Effects of axial launch spacing on cavitation interference and load characteristics during underwater salvo. *Appl. Ocean Res.* 153, 104281. doi:10.1016/j.apor.2024.104281

Gao, Z., Zhang, D., and Yi, W. (2025). Projectile trajectory and launch point prediction based on CORR-CNN-BiLSTM-Attention model. *Expert Syst. Appl.* 275, 127045. doi:10.1016/j.eswa.2025.127045

Guo, X., Liu, Q., Han, X., Li, T., Jiang, B. A., and Cai, C. (2025). High-precision numerical modeling of the projectile launch and failure mechanism analysis of projectile-borne components. *Appl. Math. Mech.* 46 (5), 885–906. doi:10.1007/s10483-025-3254-9

Hwang, D., Choi, E., and Cho, K. (2025). Usability test for an over-ground walking assistance robotic device based on the mecanum wheel. *Appl. Sci.* 15 (10), 5294. doi:10.3390/app15105294

Joksić, S., Radojković, M., Šarkoćević, Ž., Milojević, S., and Stojanović, B. (2023). Stress analysis of gear shift fork with mass optimization. In: XII international conference on social and technological development; June 15-18, 2023; Trebinje, Republic of Srpska, Bosnia and Herzegovina: STED. p. 459–464. Available online at: https://stedconference.com.

Krenn, C., and Schlicke, D. (2025). Crack width simulation with discrete reinforcement and 3D nonlinear finite element models. *Eng. Struct.* 332, 120122. doi:10.1016/j.engstruct.2025.120122

Lee, W., Joo, H., Kang, Y. K., and Seo, T. (2025). A review on the force sensing and force feedback-based navigation of Mobile robots. *Int. J. Precis. Eng. Manuf.* 26, 1291–1311. doi:10.1007/s12541-025-01244-3

Li, H., and Li, Y. (2025). Finite element analysis and structural optimization design of multifunctional robotic arm for garbage truck. *Front. Mech. Eng.* 11, 1543967. doi:10.3389/fmech.2025.1543967

Li, M., Xu, J., Wang, Y., Chen, T., and Zhang, X. (2025). Accurate analytical model for interior ballistics trajectory prediction in piston-pump-driven underwater launch systems. *J. Eng. Res.* doi:10.1016/j.jer.2025.04.003

Liu, X., Li, Y., Cheng, Y., and Cai, Y. (2023). Sparse identification for ball-screw drives considering position-dependent dynamics and nonlinear friction. *Robotics Computer-Integrated Manuf.* 81, 102486. doi:10.1016/j.rcim.2022.102486

Liu, X., Sun, Y., Wen, S., Cao, K., Qi, Q., Zhang, X., et al. (2024a). Development of wheel-legged biped robots: a review. *J. Bionic Eng.* 21 (2), 607–634. doi:10.1007/s42235-023-00468-1

Liu, Z., Wang, G., Rui, X., Wu, G., Tang, J., and Gu, L. (2024b). Modeling and simulation framework for missile launch dynamics in a rigid-flexible multibody system with slider-guide clearance. *Nonlinear Dyn.* 112 (24), 21701–21728. doi:10.1007/s11071-024-10182-0

Lu, H., Li, C., Liu, C., Hua, C., Hao, J., Xu, M., et al. (2024). Nonlinear dynamic analysis of high-speed precision grinding considering multi-effect coupling. *Int. J. Mech. Sci.* 282, 109604. doi:10.1016/j.ijmecsci.2024.109604

Maxa, J., Šabacká, P., Bayer, R., Binar, T., Bača, P., Švecová, J., et al. (2025). The tuning of a CFD model for external ballistics, followed by analyses of the principal influences on the drag coefficient of the. 223 rem caliber. *Technologies* 13 (5), 190. doi:10.3390/technologies13050190

Nikolić, V., Dolićanin, Ć., Radojković, M., and Dolićanin, E. (2015). Stress distribution in an anisotropic plane field weakened by an elliptical hole. *Tech. Gaz.* 22 (2), 329–335. doi:10.17559/TV-20131102132713

Pu, C., Jia, Y., Zhang, Z., Luo, H., Ren, M., Wang, J., et al. (2025). Intelligent optimization of air-floating piston core parameters for homemade frictionless pneumatic actuators based on a new multi-objective particle swarm optimization algorithm with gaussian mutation and fuzzy logic. *Eng. Appl. Artif. Intell.* 154, 111053. doi:10.1016/j.engappai.2025.111053

Rongzhou, L. I. N., Shuangxing, R. E. N., Lei, H. O. U., Zhonggang, L. I., Yushu, C. H. E. N., Nasser, A. S., et al. (2025). Nonlinear vibration and stability analysis of an aero-engine dual-rotor system subjected to high-frequency excitation. *Chin. J. Aeronautics* 38, 103551. doi:10.1016/j.cja.2025.103551

Serrao, P., Dhimole, V. K., and Cho, C. (2021). Effect of ankle torque on the ankle–foot orthosis joint design sustainability. *Materials* 14 (11), 2975. doi:10.3390/ma14112975

Silva-Rivera, U. S., Zuniga-Avilés, L. A., Vilchis-González, A. H., Tamayo-Meza, P. A., and Wong-Angel, W. D. (2021). Internal ballistics of polygonal and grooved barrels: a comparative study. *Sci. Prog.* 104 (2), 00368504211016954. doi:10.1177/00368504211016954

Srinivasarao, G., Samantaray, A. K., and Ghoshal, S. K. (2021). Bond graph modeling and multi-body dynamics of a twin rotor system. *Proc. Institution Mech. Eng. Part I J. Syst. Control Eng.* 235 (1), 117–144. doi:10.1177/0959651819899267

Tan, W., Wu, J., Liu, Z., Wu, X., and Zhang, J. (2023). Research on nonlinear dynamic characteristics of high-speed gear in two-speed transmission system. *Sci. Rep.* 13 (1), 20655. doi:10.1038/s41598-023-47981-1

Tang, J., Wang, G., Wu, G., Sun, Y., Gu, L., and Rui, X. (2025). Launch dynamics modeling and simulation of box-type multiple launch rocket system considering plane clearance contact. *Def. Technol.* 47, 105–123. doi:10.1016/j.dt.2024.12.016

Tian, Z., Guo, X., Ma, W., and Xue, X. (2025). Research on kiwifruit harvesting robot worldwide: a solution for sustainable development of kiwifruit industry. *Smart Agric. Technol.* 10, 100792. doi:10.1016/j.atech.2025.100792

Xin, Y., Zhu, J., Meng, K., and Jiang, S. (2025). Nonlinear dynamics study of hybrid mechanism considering three-dimensional revolute joint clearance. *Nonlinear Dyn.* 113, 16245–16275. doi:10.1007/s11071-025-10985-9

Yepez-Figueroa, J. J., Victores, J. G., Oña, E. D., Balaguer, C., and Jardón, A. (2025). Design and development of an omnidirectional three-wheeled industrial Mobile robot platform. *Appl. Sci.* 15 (10), 5277. doi:10.3390/app15105277

Zhang, J. (2025a). Application and development of artificial intelligence and computer technology in the field of intelligent robots. *Sci. Rep.* 15 (1), 14656. doi:10.1038/s41598-025-93926-1

Zhang, J. (2025b). ACP-MO: a novel metaheuristic optimization algorithm based on an advanced ceramic processing metaphor for optimization. *Appl. Eng. Lett.* 10 (2), 109–124. doi:10.46793/aeletters.2025.10.2.5

Zhang, Z., and Ma, X. (2024). Friction-induced nonlinear dynamics in a spline-rotor system: numerical and experimental studies. *Int. J. Mech. Sci.* 278, 109427. doi:10.1016/j.ijmecsci.2024.109427

Zhang, S., Rui, X., Yu, H., and Dong, X. (2024). Study on the coupling calculation method for the launch dynamics of a self-propelled artillery multibody system considering engraving process. *Def. Technol.* 39, 67–85. doi:10.1016/j.dt.2024.04.011

Zhang, X., Zhou, N., Zhang, H., Li, D., Hua, Y., Xu, C., et al. (2025a). Simulation analysis of the motion accuracy of the ECRH launcher steering mechanism based on ADAMS. *Fusion Eng. Des.* 211, 114774. doi:10.1016/j.fusengdes.2024.114774

Zhang, Z., Liang, K., Pan, M., Wang, H., Sang, H., Zhou, S., et al. (2025b). Exhaust emissions prediction in spark ignition engine using LightGBM optimized with the marine predators algorithm. *Appl. Therm. Eng.* 275, 126800. doi:10.1016/j.applthermaleng.2025.126800

Zhizhong, C., Hongqing, L., Zengcong, L., Yan, C., Jie, C., and Xiaoqi, L. (2023). Structural lightweight design and experimental validation for aerospace sealed cabin. *Front. Mech. Eng.* 9, 1265734. doi:10.3389/fmech.2023.1265734

Zhou, B., Wang, J., Feng, P., Zhang, X., Yu, D., and Zhang, J. (2025). A genetic particle swarm optimization algorithm for feature fusion and hyperparameter optimization for tool wear monitoring. *Expert Syst. Appl.* 285, 127975. doi:10.1016/j.eswa.2025.127975

Zikri, J. M., Sani, M. S. M., Rashid, M. F. F. A., Muriban, J., and Prayogo, G. S. (2025). Predictive modeling and optimization of noise emissions in a palm oil methyl ester-fueled diesel engine using response surface methodology and artificial neural network integrated with genetic algorithm. *Int. J. Thermofluids* 26, 101103. doi:10.1016/j.ijft.2025.101103

## Nomenclature

| | |
|---|---|
| $\boldsymbol{\sigma}$ | Cauchy stress tensor |
| $\boldsymbol{b}$ | Force |
| $\boldsymbol{\rho}$ | Material density |
| $\ddot{\boldsymbol{u}}$ | Acceleration vector |
| $\boldsymbol{\delta u}$ | Test function |
| $\boldsymbol{t}$ | Surface force |
| $\boldsymbol{\varepsilon}$ | Strain tensor |
| $\boldsymbol{W}$ | Strain energy function |
| $\boldsymbol{\lambda_i}$ | Principal stretches |
| $\boldsymbol{\mu_i}$, $\boldsymbol{\alpha_i}$ | Material parameter |
| $\boldsymbol{F_t}$ | Tangential friction force |
| $\boldsymbol{F_n}$ | Normal contact force |
| $\boldsymbol{\mu}$ | Coefficient of friction |
| $\boldsymbol{\omega_1}$, $\boldsymbol{\omega_2}$ | Friction wheel angular velocity |
| $\boldsymbol{v_1}$, $\boldsymbol{v_2}$ | Projectile initial and final velocity |
| $\boldsymbol{\Phi_1}$, $\boldsymbol{\Phi_2}$ | Friction wheel diameter |
| $\boldsymbol{\Phi_3}$ | Projectile diameter |
| $\boldsymbol{d}$ | Friction wheel gap |
| $\boldsymbol{\mu}$ | Coefficient of friction |
| $\boldsymbol{C_{10}}$, $\boldsymbol{C_{01}}$ | Mooney-Rivlin parameter |